Atomic-scale friction image of graphite in atomic-force microscopy

Naruo Sasaki, Katsuyoshi Kobayashi, and Masaru Tsukada
Department of Physics, Graduate School of Science, University of Tokyo, 7-3-1 Hongo, Bunkyo-ku, Tokyo 113, Japan
(Received 22 November 1995; revised manuscript received 28 February 1996)

We theoretically investigated the image of atomic-scale friction of graphite in atomic-force microscopy (AFM), based on numerical simulation for a static model. We performed systematic calculations of lateral force images of AFM aiming to clarify the effects of cantilever stiffness, scan direction, anisotropy of the cantilever, and surface deformation. The simulation is performed for a simple atomistic model with a single-atom tip connected with the cantilever spring scanned on a monolayer graphite surface. The process in which the conservative lateral force becomes a nonconservative frictional force is clarified. ''Stick regions'' of the tip atom are also discussed in relation to the cantilever stiffness. Calculated frictional-force image patterns are in good agreement with experimental ones. We also find the supercell frictional-force images and discuss their mechanisms. [S0163-1829(96)01727-4]

I. INTRODUCTION

Friction between two solids is an indispensable phenomenon for our daily life, and its mechanism has long been investigated by researchers ranging from fundamental to applied sciences. Recent development of atomic-force microscopy[1] (AFM) has enabled us to observe the atomic-scale friction, and has opened a new research area of friction—nanotribology.[2] Therefore AFM, which, in the measurement of friction, is usually called frictional-force microscopy, is a powerful tool for understanding the basic friction mechanism between a single asperity and an atomically flat surface. Atomic-scale frictional forces have been observed so far by AFM for the surfaces of graphite,[2–7] mica,[8–10] and transition-metal dichalcogenides.[11,12] Theoretical studies of friction in relation to AFM have been also performed by using simple physical models,[12] molecular dynamics simulations,[13–16] first-principles calculations,[17–19] and an analytical method.[20]

Recently the two-dimensional nature of the atomic-scale friction has attracted our attention, because it might reveal some important behaviors of the tip apex on the surface, which are essentially related to the origin of the friction. Fujisawa *et al.*[7,9,11] measured frictional forces both along and across the scan direction, and explained the experimental images by the ''two-dimensional stick-slip model.'' Kerssemakers and De Hosson[12] also observed the frictional-force images of transition-metal dichalcogenides, and described them based on two physical models: static (geometrical) and dynamical ones. It was shown that the observed image patterns are strongly dependent on a two-dimensional stick slip. Gyalog *et al.*[20] analytically investigated the mechanism of atomic-scale friction in terms of a two-dimensional model, and calculated the two-dimensional regions where friction occurs, in relation to cantilever stiffness and anisotropic coupling between a tip and a support.

However, from a theoretical viewpoint, the fundamental problem—how the macroscopic mechanical condition such as the cantilever stiffness has influence on lateral force images—has not been fully discussed yet. It is very important to know what kind of information is included in the most available experimental results—force images. Therefore, in the present work, we focus on the lateral force images and investigate several influences on them based on numerical simulation on a static model. We performed overall studies about the lateral force images of AFM systematically in relation to cantilever stiffness, scan direction, anisotropy of the cantilever, and surface deformation. Some of the general features of the two-dimensional atomic-scale friction in AFM are also clarified. The simulation is performed by the simple atomistic model with a single-atom tip connected with the cantilever spring scanned on a graphite monolayer surface. In this work, it is assumed that the term ''lateral force'' means the lateral component of the force F_x or F_y acting on the tip atom, irrespective of whether it is frictional or not. On the other hand, ''vertical force'' is assumed to mean the vertical component of the force F_z, vertical to the surface plane.

In Sec. II, our model and the method of the calculation are presented with the parameters of potential. In Sec. III, the results obtained by the model calculation are discussed. First, a vertical force curve is calculated, in order to clarify the condition of the normal reaction force F_z for the scanning the tip in the lateral direction. Then, we reproduce the lateral force images for various values of the cantilever stiffness. The process in which the conservative lateral force image becomes nonconservative frictional force image is clearly presented. The relation between the image pattern and the arrangement of the graphite atom is discussed. The appearance of the supercell frictional-force images and their mechanisms are also discussed. Then the mechanism of stick-slip is explained by the feature of the potential energy surface V. Further, we investigate influences on lateral force images by various parameters as scan direction, anisotropy of the cantilever and surface deformation. The simulated frictional-force images are compared to the observed ones.

II. MODEL AND METHOD OF CALCULATION

In our calculation, a single-atom tip connected with a cantilever is scanned on a monolayer graphite surface as shown in Fig. 1. The total potential energy V is assumed to consist

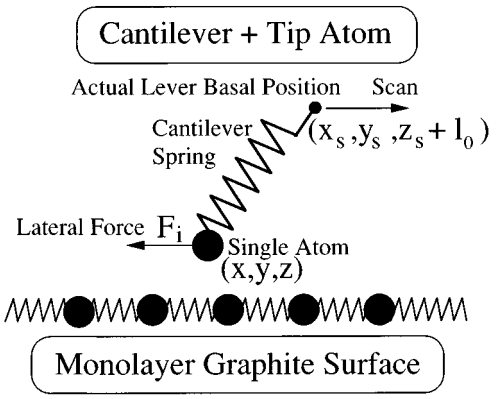

FIG. 1. Schematic illustration of the system used in our calculation. The single-atom tip connected with the cantilever spring is scanned on a monolayer graphite surface.

of the elastic energy of the cantilever V_T and surface V_S, and the microscopic tip-surface interaction V_{TS}. This relation can be written as $V=V_T+V_S+V_{TS}$. Both V_T and V_S are assumed to be harmonic. In particular, the cantilever is reproduced by an equivalent three-dimensional virtual spring.

In the simulation, the following conditions are assumed: First, it is supposed that the tip-surface system is under the condition of absolute zero point $T=0$ K. In this case, thermal activated processes can be perfectly neglected. Further, the scanning speed of the tip in the AFM experiment is much smaller than the characteristic velocity of the lattice vibration. Therefore, we can assume that the tip scanning velocity v is almost in the limit of zero. The potential energy surface of the tip-surface system for a given cantilever basal position is very slowly changed in time with the scan of the basal position. Note that the adiabatic potential surface itself evolves in time by the external force, driving the cantilever. The system is always located at an equilibrium position of the potential surface as shown in Fig. 2 for each scan point. Therefore, it is implicitly assumed that the energy of the system is supplied or removed by the external force driving the cantilever. This is schematically understood by a simple one-dimensional model shown in Fig. 2. It is assumed that the surface is rigid and that $V(x)=V_T(x)+V_{TS}(x)$. x is a direction in which the tip is moved one dimensionally on the surface. By changing the stiffness of the cantilever, two types of potential energy surfaces appear as shown in Figs. 2(a) and 2(b). For the stiff cantilever, the total energy V is nearly parabolic and only a single minimum appears. However, for the soft cantilever, several metastable points corresponding to local minima appear. Thus the appearance of the case of Fig. 2(a) or Fig. 2(b) is determined by the ratio between the magnitude of the spatial variation of V_T and V_{TS}.

Therefore, for the stiff cantilever, the representative point of the system (the tip atom in this case) is always moving trapped in a minimum of the potential energy surface and shifts continuously [Fig. 2(a)]. On the other hand, for the soft cantilever, discontinuity of the motion of the tip atom occurs as shown in Fig. 2(b). In this case, for some period of the cantilever scan, the tip atom is moving continuously. But it makes a sudden jump from one minimum to another deeper minimum, when the barrier between two minima disappears. The system energy is dissipated instantaneously when the tip

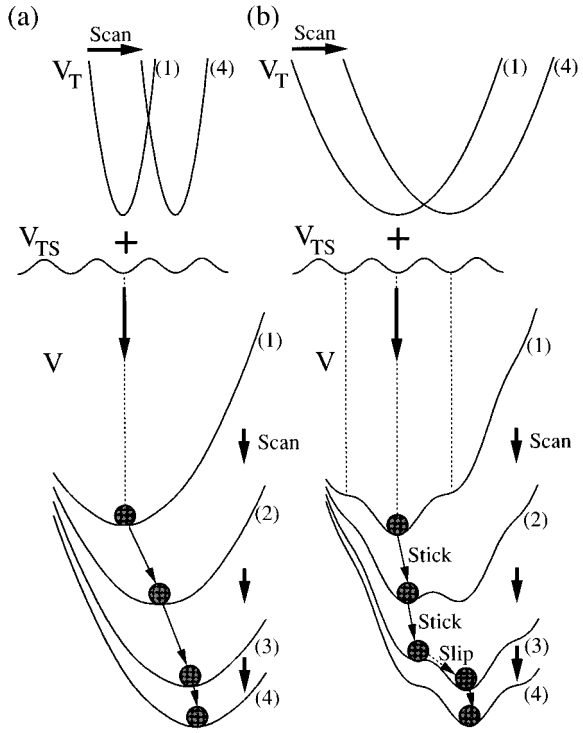

FIG. 2. Schematic illustration of the total energy V obtained by the sum of the elastic energy of the cantilever spring V_T and the tip-surface interaction V_{TS}. Two cases for a (a) stiff and (b) soft cantilever are presented. (1)–(4) denote the time evolutions of the potential by the tip scan. For the stiff cantilever, total energy V is nearly parabolic, and the tip atom (the shaded circle) is always located at the minimum. However, for the soft cantilever, several metastable points corresponding to local minima appear, and the tip atom jumps to the deeper minimum at these points, when the barrier between two minima disappears.

atom slips from a local potential minimum to another. This mechanism of energy dissipation is only an assumption we make and it is not necessarily correct from the standpoint of the dynamics. Nevertheless, in this work, we discuss various features of atomic-scale friction based on this mechanism.

Here, the details of the potential are described. First, V_T is expressed as follows:

$$V_T=\tfrac{1}{2}[k_x(x-x_s)^2+k_y(y-y_s)^2+k_z(z-z_s)^2], \qquad (1)$$

where $k_i(i=x,y,z)$ is an elastic constant of the cantilever spring parallel to the $i(i=x,y,z)$ direction. This spring is also assumed to include the effect of the microscopic interatomic bonds of the tip. (x,y,z) denotes the actual tip atom position, and (x_s,y_s,z_s) denotes the equilibrium position of the tip atom for the system without the interaction with the surface. We call (x_s,y_s,z_s), ''the lever basal position,'' hereafter.

Here the x and y directions parallel to the surface are defined as shown in Fig. 3 and the z axis is perpendicular to the surface x-y plane. The origin of the z axis is defined as the position of the graphite surface before deformation. The vertical component k_z is assumed to be 0.25 N/m, which is of the same order as realized in experimental works. k_x and k_y are assumed to be parameters.

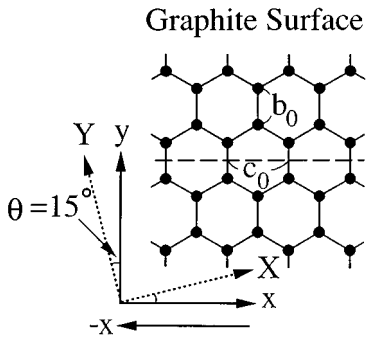

FIG. 3. The schematic view of the lattice structure of the graphite. c_0 is the length of a unit translational vector of graphite. b_0 is the C-C bond length of graphite. c_0=2.46 Å, and b_0=1.42 Å. The X or Y axis is obtained by rotating the x or y axis 15° counterclockwise around the origin (hollow site).

Similarly, V_S is assumed to consist of three types of harmonic terms as follows:

$$V_S=\frac{1}{2}\sum_{i-j}\mu_r(r_{ij}-r_0)^2+\frac{1}{2}\sum_{i-j-k}\mu_\theta r_0^2(\theta_{ijk}-\theta_0)^2+\frac{1}{2}\sum_{i-(j,k,l)}\mu_p\left(\delta z_i-\frac{\delta z_j+\delta z_k+\delta z_l}{3}\right)^2. \quad (2)$$

This potential was used by Yoshimori and Kitano[21] in order to study the lattice vibration and specific heat of graphite. The indices of the summation $i-j$, $i-j-k$, and $i-(j,k,l)$ represent the nearest-neighbor bonds, bond pairs, and bond triples, respectively. The first and the second term correspond to the bond stretching, and the bond bending energy, respectively. r_{ij} is the nearest-neighbor bond length between the bond i-j. θ_{ijk} denotes the angle between the bond i-j and the bond j-k within the same honeycomb net plane. The third term is the bending energy of the local planar structure due to the normal displacement of the ith atom from the coplanar position with respect to the three neighboring atoms j, k, and l; δz_i denotes the normal displacement of the ith atom from the initial position. As monolayer graphite is treated, the interlayer bond stretching energy is neglected. The parameters of V_S are assumed as r_0=1.4210 Å, μ_r=41.881 eV/Å^2, $\theta_0=2\pi/3$ rad, μ_θ=2.9959 eV/Å^2, and μ_p=18.225 eV/Å^2, respectively.

The model of the graphite monolayer surface consists of 600 carbon atoms and 271 hexagons, and the lattice constant of the graphite is assumed to be 1.421 Å. The center of the hexagon is called the hollow site hereafter. First, this graphite surface is assumed to be rigid and V_S is neglected in Secs. III A–III D, in order to examine the tip-induced dry friction. Then in Sec. III E, the surface is allowed to deform by the potential model V_S, in order to examine the effect of surface deformation. In this case, the range of the tip scan will be limited near the center of the surface model, to avoid the artificial boundary effect.

Tip-surface interaction V_{TS} can be obtained as the sum of all the pair interactions between the single-atom tip and the substrate surface atoms. The Lennard-Jones potential is employed as each interatomic interaction as follows:

$$V_{TS}=\sum_i 4\epsilon\left[\left(\frac{\sigma}{r_{0i}}\right)^{12}-\left(\frac{\sigma}{r_{0i}}\right)^{6}\right]. \quad (3)$$

Here, r_{0i} is the distance between the tip atom and the ith atom in the graphite surface, and the parameters are assumed to be $\epsilon=0.87381\times10^{-2}$ eV, σ=2.4945 Å. This interaction potential with these parameters can be excellently reproduce the corrugation amplitude of AFM images of the graphite.[22–24]

The simulation has been performed under the constant-height mode. Therefore, (x_s,y_s) is varied with z_s fixed, and the total energy V is minimized for each (x_s,y_s), based on the Polak-Ribiere–type conjugate gradient method.[25] Then the optimized position of the tip atom (x,y,z), and the lateral force $F_i(i=x,y)$ acting on the lever basal position are obtained. The lateral force F_i acting in the $-i$ direction, as defined in Fig. 1, is given by

$$F_i=\left.\frac{\partial V}{\partial x_i}\right|_{(x,y,z)=(x_s,y_s,z_s)} \quad (i=x,y). \quad (4)$$

Here, z_s is an equilibrium tip-atom position measured from the surface for the system without the tip-surface interaction as mentioned before. The deflection of the cantilever Δz is defined as $\Delta z=z_s-z$. It should be remarked that the distance z_d between the actual lever basal position and the surface is defined according to the natural length of the cantilever spring. If the natural spring length in the z direction is l_0, z_d is represented as z_s+l_0, for the rigid surface. Then, in a constant-height mode, the tip is scanned in the condition of z_d=const, or equivalently in the condition of z_s=const. In our calculation, the tip is scanned at the constant-height mode with $z_d=l_0-6$ Å, that is to say, $z_s=-6$ Å. Under this condition, the average normal reaction force $\langle F_z\rangle$ is repulsive and it is about 0.21 nN.

III. RESULTS OF CALCULATIONS

A. Vertical force curve

First, the vertical force F_z curve is calculated. Then the mechanism of hysteresis in the vertical direction is described. Figure 4 is a z_s-$F_z(z_s)$ relation on the hollow site. A horizontal axis represents the lever basal position z_s. Solid and dotted curves correspond to the force curve for approaching or retracting the lever basal position, respectively. Hysteresis appears in this force curve. The lever basal position is moved in the order of $a\rightarrow c\rightarrow d\rightarrow e\rightarrow c'\rightarrow b\rightarrow a$, on the force curve, as shown in Figs. 4(a)–(e) correspond to z_s=7.5 Å (a), 7.0 Å (b), 6.0 Å (c) or (c′), 5.2 Å (d), and 4.5 Å (e), respectively. In our simulation, when the cantilever deflection $\Delta z=z_s-z<(>)\,0$, the tip atom receives repulsive (attractive) force $F_z>(<)\,0$. Adsorption force with which the tip atom is stuck onto the surface is about −0.066 nN, and the adhesive force with which the tip atom is retracted from the surface is about 0.11 nN. These forces are one or two orders smaller than those observed in UHV or air, respectively. This discrepancy arises because our model includes neither the contamination layer such as water and other gas molecules, nor long-range attractive forces reflecting the macroscopic tip shape.

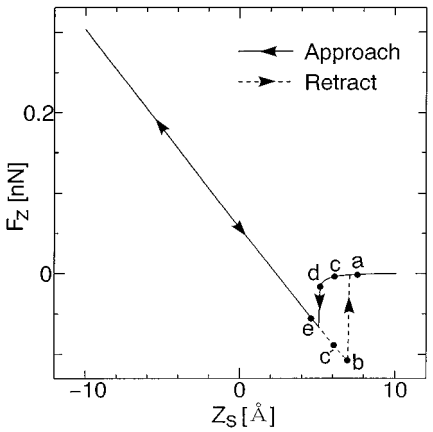

FIG. 4. Force curve of the z_s-F_z relation on the hollow site with k_z=0.25 N/m. The solid line denotes F_z when the tip approaches the surface. The dotted line denotes F_z when the tip is retracted from the surface. The lever basal position is moved in the order of $a\rightarrow c\rightarrow d\rightarrow e\rightarrow c'\rightarrow b\rightarrow a$. z_s=(a) 7.5, (b) 7.0, (c) or (c′) 6.0, (d) 5.2, and (e) 4.5 Å.

The behavior of the hysteresis of the force curve can be explained from the total energy $V=V(z;z_s)$ on the hollow site. When the lever basal position approaches the surface, the tip atom is at first located at the local minimum (Figs. 5 curves $a-e$) and F_z varies continuously with z_s. The curves labeled $a-e$ in Fig. 5 correspond to the z_s positions marked in Fig. 4, respectively. At z_s=5.2 Å [the case of d], the tip atom suddenly jumps from one minimum to another deeper minimum, because the barrier between the two minima disappears (Fig. 5, curve d). Here, the jump of the force curve appears as shown by the solid curve of Fig. 4. In this case, the tip atom is adsorbed onto the surface. Just after this adsorption, the F_z is attractive. But as the lever basal position approaches the surface further, F_z becomes repulsive at z_s=2.3 Å. Our simulations for lateral force images are performed under the constant height $z_s=-6$ Å with the repulsive force F_z as mentioned in Sec. II.

On the other hand, when the tip atom is retracted from the surface, the position where the tip atom makes a sudden jump appears at z_s=7.0 Å (Fig. 5, curve b). Thus the position where the tip atom jumps for the tip retraction is different from that for the tip approach. This is the mechanism of the hysteresis from the viewpoint of the adiabatic total potential V. As will be seen later, the two-dimensional stick-slip motion during the tip scan takes place by the similar mechanism.

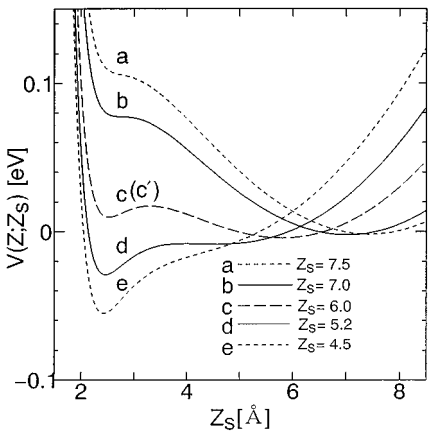

FIG. 5. One-dimensional adiabatic potential $V(z;z_s)$ in the case of Fig. 4. z_s=(a) 7.5, (b) 7.0, (c) or (c′) 6.0, (d) 5.2, and (e) 4.5 Å.

B. Cantilever stiffness and mechanism of stick-slip

In this section, the influence of the cantilever stiffness on lateral force images are systematically investigated. Here, we will find that the effect on the friction image of changing the cantilever stiffness is almost equivalent to that by changing the tip-surface interaction. For example, a soft cantilever corresponds to a strong tip-surface interaction or a large load F_z.

1. Lateral force images

Two-dimensional lateral force images are calculated for various values of cantilever stiffness. The width of each mesh of the scan point is $c_0/40$=0.0614 Å in the x direction. Here, c_0 is the length of a unit translational vector of graphite as shown in Fig. 3. If this x scan is repeated in the y direction, the two-dimensional lateral force image is constructed. The width of each mesh of the scan point in the y direction is $b_0/10$=0.142 Å. b_0 is the C-C bond length of graphite as shown in Fig. 3. The scanning region of the lever basal position is 9.8 Å×8.5 Å. The tip is scanned under the constant height mode of $z_s=-6$ Å, with $\langle F_z\rangle\simeq$0.21 nN.

Here it should be noted that the initial condition for the start of the scan is assumed as $x=x_s=0$ and $y=y_s$ in our calculations. Therefore at the start point of each scan line before relaxation, the tip atom is located at the same x-y position as the lever basal position. Then the tip atom is totally relaxed after optimization. Although this start condition is different from that usually employed in experiments, we use the start condition in calculating lateral force images in this work.

This procedure is repeated for several kinds of cantilever stiffness. The isotropic cantilever spring of $k_x=k_y=k$ is used. For each k, both x and y components of lateral forces are obtained. Figures 6(a)–6(f). are calculated lateral force images for k=2.5 (a), 1.5 (b), 1.0 (c), 0.75 (d), 0.50 (e), and 0.25 N/m (f), respectively. The rightmost figures for (b)–(f) represent the shapes of the boundary where the brightness rapidly changes from maximum to minimum in F_y. Cantilever spring constants k_x and k_y mentioned above are two or three orders of magnitude smaller than those in experiments. One reason for this problem, weak spring, is that our model adopts a single-atom tip model, which detects much smaller force than the experimental one. Therefore we must use weak spring. However, Abraham and Batra[26] pointed out that the flake tip actually detects force on the graphite surface in contact-AFM experiments. If the calculation is performed by the flake tip including a large number of carbon atoms, we must use a spring that is as strong as that in experiments. The other reason is that the effective spring constant becomes small during the scanning by the flexing of the tip apex. Griffith and Grigg[27] pointed out the possibility of the flexing of the tip apex by the lateral force.

Solid curves in Fig. 7 show the cross sections of F_x in Fig. 6 at the line indicated by the thick arrows along the x

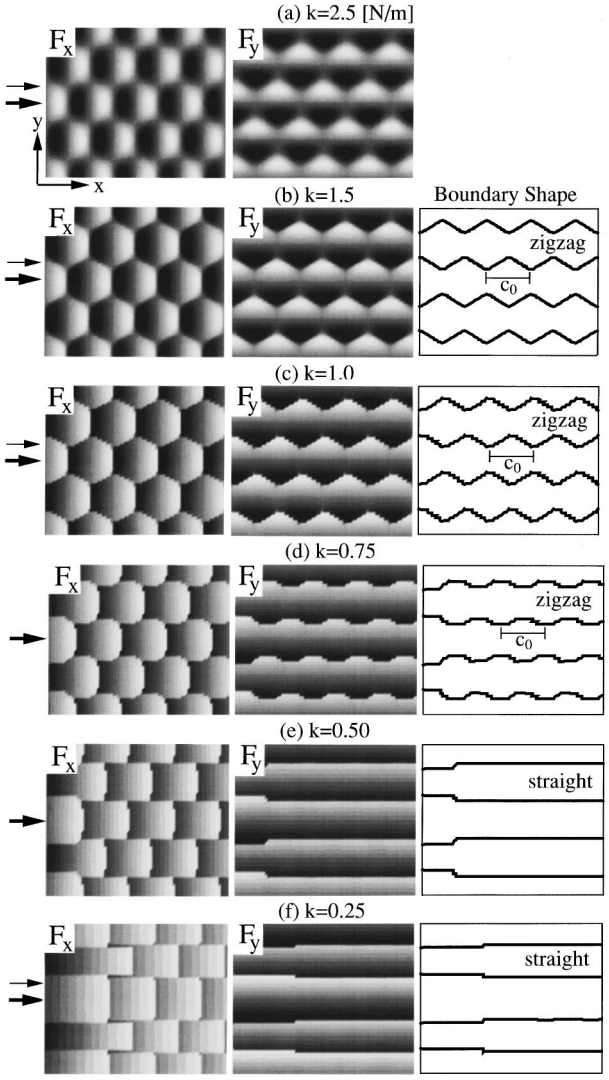

FIG. 6. Lateral force images of F_x and F_y, with the tip scanned in the x direction of Fig. 3. The rightmost figures represent the shape of the boundary where the brightness rapidly changes from maximum to minimum in F_y. Spring constants $k_x=k_y=k=$(a) 2.5, (b) 1.5, (c) 1.0, (d) 0.75, (e) 0.50 and (f) 0.25 N/m. The scanning region is 9.8 Å×8.5 Å.

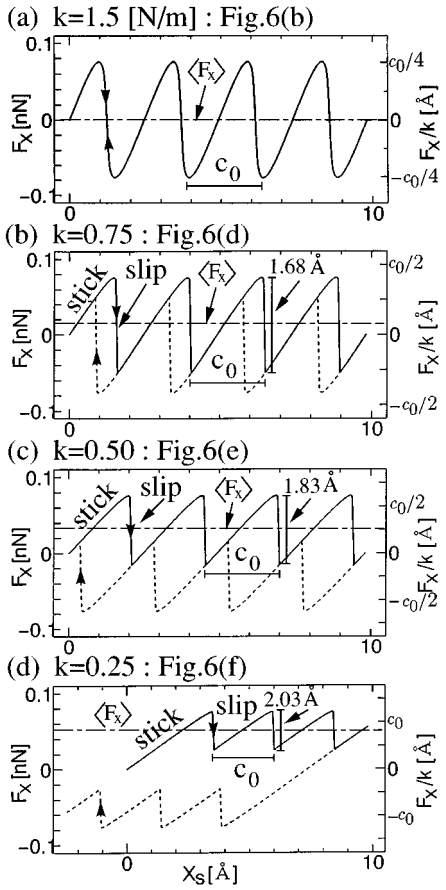

FIG. 7. The cross sections of F_x in Fig. 6 at the line indicated by the thick arrows along the x direction. They mean lateral force curves of the x_s-F_x relation. Spring constants $k_x=k_y=k=$(a) 1.5, (b) 0.75, (c) 0.50, and (d) 0.25, N/m. The left-hand vertical axis means $F_x(x_s)$, and the right-hand one means the cantilever deflection in the x direction, $F_x(x_s)/k$. The solid and dotted line correspond to the force curve with the tip scanned in the x and $-x$ direction, respectively. The average lateral force $\langle F_x\rangle$ for the x scan is represented by dot-dashed lines. c_0 is the length of a unit translational vector of graphite, as shown in Fig. 3, and $c_0=2.46$ Å.

direction. Figures 7(a), 7(b), 7(c), and 7(d) correspond to Figs. 6(b), 6(d), 6(e), and 6(f), respectively. These cross sections mean $x_s-F_x(x_s)$ relations with the lever basal position scanned along the x direction on the broken line in Fig. 3. In Fig. 7, the left-hand vertical axis means $F_x(x_s)$, and the right-hand one means the cantilever deflection in the x direction, $F_x(x_s)/k$. Dotted curves in Figs. 7(a)–7(d) are obtained by the $-x$ scan. In Fig. 7(a), hysteresis is not observed in the force curve. In this case, F_x is frictionless and conservative, and it is defined only by the lever basal position x_s. Furthermore, it can be shown that

$$\langle F_x\rangle=\frac{1}{c_0}\int_0^{c_0}F_x(x_s)dx_s=0,$$

directly indicating the absence of dynamic friction. However, when the cantilever becomes soft, the force curves show sawtooth behavior with a discontinuous jump corresponding to the slip motion of the tip atom, as shown in Figs. 7(b)–7(d). In these cases, hysteresis is clearly observed, and it becomes more remarkable as the cantilever becomes softer. Therefore, F_x becomes nonconservative, that is to say, $\langle F_x\rangle\neq 0$, indicating the appearance of the dynamic frictional force. For $k=1.5$, 0.75, 0.50, and 0.25 N/m, $\langle F_x\rangle\simeq 0$, 0.018, 0.034, and 0.052 nN, as shown in dot-dashed lines of Figs. 7(a)–7(d), respectively. The value of $\langle F_x\rangle$ as a function of k is presented in Fig. 8 for 0.5 N/m$\leqslant k\leqslant$1.5 N/m. As seen in this figure, $k_c\simeq 1.3$ N/m is a critical value of the cantilever stiffness for the appearance of a finite value of $\langle F_x\rangle$. F_y equals 0 on the broken line in Fig. 3 because of the symmetry of the graphite lattice.

Thus it can be said that Figs. 6(a) and 6(b) for $k>k_c$, are conservative force (frictionless) images and Figs. 6(d)–6(f) for $k<k_c$, are nonconservative force (frictional force) images. It should be remarked, however, that the critical value of k_c varies by the y coordinate where the x scan is performed. The feature of the image pattern of Fig. 6(e), especially the periodicity, is very similar to that of the experimental image observed by Fujisawa *et al.*[7] [see Fig. 1(b) in

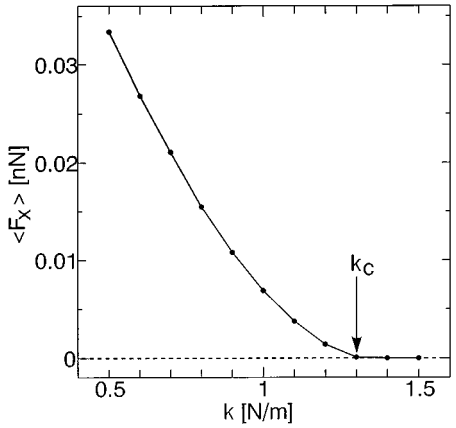

FIG. 8. The relation between the cantilever stiffness k and average lateral force $\langle F_x \rangle$, for the scan on the broken line in Fig. 3. $k_c \simeq 1.3$ N/m is a critical value of the cantilever stiffness for the appearance of a finite value of $\langle F_x \rangle$.

Ref. 7 under the constant height mode. For example, the calculated sawtooth periodicity of the cross section indicated by a thick arrow in Fig. 6(e) along the x direction [the lateral force curve Fig. 7(c)], is $c_0 = 2.46$ Å, which agrees well with the experimental one, 2.5 ± 0.3 Å.[7] Thus it is confirmed that our simple atomistic model can reproduce experimental frictional-force images. However, we cannot reproduce the cantilever spring constant k and the load F_z quantitatively. Therefore the calculated corrugation amplitude 1.83 Å of the images is different from the experimental one 2.5 ± 0.3 Å.[7] In this point it can be concluded that the agreement between our calculation and experiments is qualitative.

2. Features of image patterns

In the following, features of image patterns of Figs. 6(a)–6(f) are described in more detail. For $k = 2.5$ N/m corresponding to Fig. 6(a), the cantilever spring is so stiff that the effect of it hardly appears, thus Fig. 6(a) almost reflects the tip-surface interaction V_{TS} itself. However, for $k = 1.5$ N/m corresponding to Fig. 6(b), the effect of the cantilever becomes enhanced, and the image of Fig. 6(b) considerably deforms compared to Fig. 6(a). The honeycomb lattice in Fig. 6(b) corresponds perfectly to the network of the graphite bonds. The relation between the image pattern in Fig. 6 and the arrangement of the graphite atom is discussed below. Figures 9(a) and 9(b) represent the relation between the graphite atom site and the cross section of F_x in Figs. 6(b) and 6(e) at the line indicated by a thick arrow. The lateral force F_x and the total energy V are shown in relation to the graphite atom sites—hollow sites (white circles) and C-C bond sites (black circles). As seen in Fig. 9(a), the total energy V varies continuously. Then V takes a maximum at the C-C bond site, and a minimum at the hollow site, that is to say, F_x equals 0 at both the hollow sites and C-C bond sites. Further, it can be clearly shown that $F_{\max}$ and $F_{\min}$ are located symmetrically around the C-C bond site. Therefore the sharp boundary between the positive (bright) and the negative (dark) F_x regions appears as the network line of the honeycomb lattice corresponding to the graphite bonds. In both F_x and F_y in Fig. 6(b), the C-C bonds of the graphite that are not parallel to the y axis make zigzag patterns. These

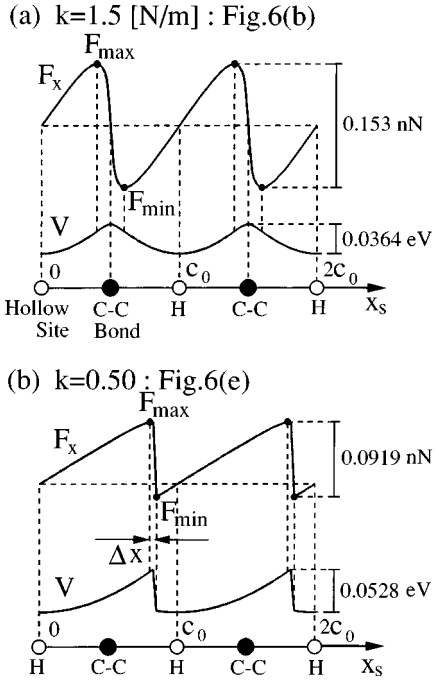

FIG. 9. The relation between the lateral force F_x and graphite atomic sites, in relation to the total energy V. F_x's are cross sections of Fig. 6 at the line indicated by the thick arrows along the x direction. White and black circles mean hollow sites and C-C bond sites, respectively. c_0 is 2.46 Å. Spring constants $k_x = k_y = k =$ (a) 1.5 and (b) 0.50 N/m. Δx in (b) is $c_0/20$ Å, indicating the width of two meshes of the scan point.

zigzag patterns consist of zigzag lines with periodicity of c_0 along the x direction as shown in the rightmost figure of Fig. 6(b).

With further decrease of the value of k, we get into the nonconservative force image regime, then two kinds of drastic changes of the image occur: one is the disappearance of the zigzag pattern, and the other is the shift of the position of the maximum or the minimum of F_x. First, the rapid change of the zigzag pattern is described. At first, zigzag patterns comprised of zigzag lines with the periodicity of c_0 are clearly observed in the rightmost figure of Fig. 6(c). However, these patterns decrease as the cantilever spring becomes soft, as shown in the rightmost figure of Fig. 6(d). Eventually, zigzag patterns vanish perfectly in the rightmost figure of Fig. 6(e). Figures 6(e) and 6(f) have only straight shaped images parallel to the x axis. The reason for these changes will be explained based on the two-dimensional distribution of the tip atom in Sec. III B 4.

Then the shift of the position of the maximum or the minimum of F_x is mentioned. As seen in Fig. 9(b), the total energy V varies discontinuously, and the discrete jump between $F_{\max}$ and $F_{\min}$ occurs. Because of the stick of the tip atom, $F_{\max}$ and $F_{\min}$ shift in the x direction. Therefore in Fig. 9(b), $F_{\max}$ and $F_{\min}$ do not appear symmetrically with respect to the C-C bond, although the image pattern itself has the periodicity of the C-C bond length of the graphite. The feature and mechanism of the stick-slip are mentioned in Sec. III B 5.

3. Supercell feature of images

Further, we find a strange supercell feature as seen in Fig. 6(f). When we pay attention to the variation of the image

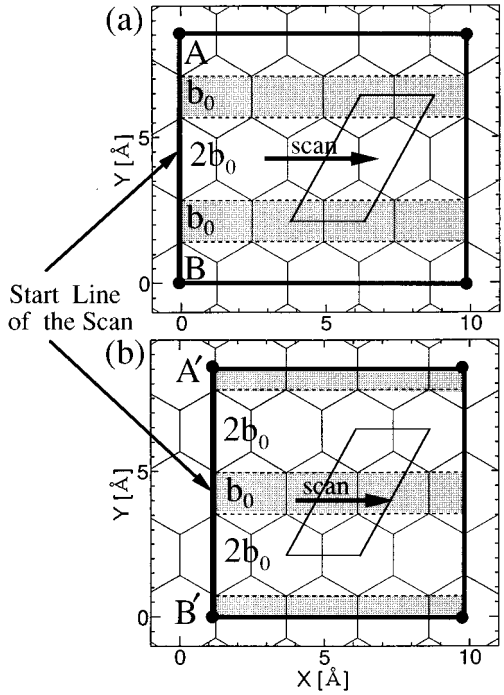

FIG. 10. Schematic illustration of two kinds of supercell frictional force images of F_x for $k=0.25$ N/m. The start line of the scan $A'B'$ in (b) is obtained by shifting AB in (a) by 1.23 $(=c_0/2)$ Å, in the x direction. The masked area has the width of 1.42$(=b_0)$ Å in the y direction. The frame made by a thick straight line means the scan region, corresponding to Fig. 6(f). The rhomboids represented by the solid lines show 1×2 supercell structures with respect to the unit cell of the graphite lattice.

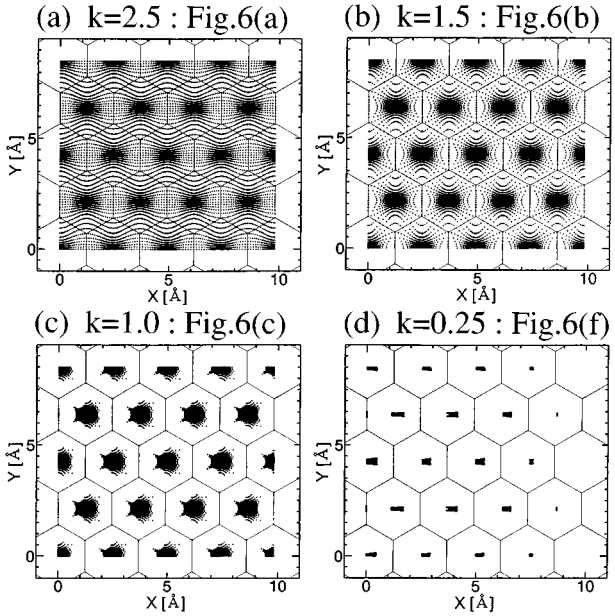

FIG. 11. Two-dimensional distribution of the tip atom. Each dot is the position of the tip atom after each minimization of V, and solid lines represent C-C bonds of the graphite surface. Spring constants $k_x=k_y=k=$(a) 2.5, (b) 1.5, (c) 1.0, and (d) 0.25 N/m. The scanning region is 9.8 Å×8.5 Å. Stick regions appear in (c) and (d).

pattern in the y direction, it can be noticed that the same pattern appears in the cycle of b_0 and $2b_0$. Therefore the frictional force image has a 1×2 supercell symmetry with respect to the unit cell of the graphite lattice. The periodicity in the y direction and the supercell are presented by schematic illustrations in Fig. 10(a). The frame made by the thick straight line means the scan region, corresponding to Fig. 6(f). As shown in Fig. 10(a), the periodicity of b_0 and $2b_0$ in the y direction corresponds to the graphite atom spacing on the start line AB of the x scan. When we shift the start line of the scan AB of Fig. 10(a) to the position $A'B'$ of Fig. 10(b), an image different from Fig. 10(a) is obtained. The appearance of the two alternative long period images is a remarkable feature for the soft tip cases and it is caused by the two-dimensional stick-slip hysteresis motion of the tip atom.

4. Two-dimensional distribution of the stick region

Since the feature of the image patterns mentioned in Sec. III B 2 can be explained by the motion of the tip atom, the behavior of the tip atom during the scan is investigated below. In order to know clearly where the tip atom sticks, and between which site it slips, we also calculate the optimized positions of the tip atom (x,y). The scanning region of the lever basal position is 9.8 Å×8.5 Å. Figures 11(a)–11(d) are obtained by plotting (x,y), corresponding to the cases of $k_x=k_y=k=2.5$ (a), 1.5 (b), 1.0 (c), and 0.25 N/m (d), respectively. In these figures, each dot represents the position of the tip atom after each minimization of V, and solid lines represent C-C bonds of the graphite lattices. For $k>k_c$, the tip atom is distributed continuously over the entire x-y plane [Figs. 11(a) and 11(b)]. However, with the decrease of k, the density of the distribution of the tip atom around the hollow site becomes large. Finally, for $k<k_c$, the tip atom exists only around the hollow site [Figs. 11(c) and 11(d)], indicating the appearance of the stick-slip motion. The stick regions become smaller as the cantilever becomes softer, as shown in Figs. 11(c) and 11(d). Therefore it is clearly demonstrated that the atomic-scale dynamic friction is due to the two-dimensional stick-slip motion of the tip atom.

In the z direction, stick regions are distributed over only about 0.20 Å around $z\simeq2.2$ Å. Therefore it can be concluded that the stick regions are distributed over a pancake-shaped region parallel to the surface, because of the flatness of the graphite surface. The stick regions make triangular lattices as a whole, and each of them is located above the hollow site of graphite. These results are in good agreement with the picture of the two-dimensional stick-slip model inferred by Fujisawa *et al.*[7,9,11] This concept of the two-dimensional friction from the standpoint of the cantilever stiffness was also discussed theoretically by Gyalog *et al.*[20]

Here the variation of the image pattern mentioned in Sec. III B 2 is simply explained using the two-dimensional tip-atom distribution. We focus on the scan that intersects the C-C bonds tilted by 30° or 150° from the x axis. Then the tip-atom position (x,y) for this scan line is presented as shown in Fig. 12. The position of the scan line (broken line in Fig. 12) is $x_s\geqslant0$ and $y_s=3.7c_0$, corresponding to the position indicated by the thin arrows along the x direction in Figs. 6(a), 6(b), 6(c), and 6(f). Each dot connected by the line represents the continuous tip-atom motion for $k=2.5$ (a) and 1.5 N/m (b), and the stick motion for $k=1.0$ (a) and 0.25 N/m (b), respectively.

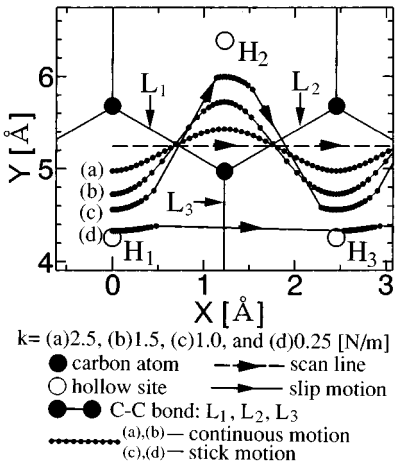

FIG. 12. The part of Fig. 11, corresponding to the tip-atom position (x,y) for the scan line which intersects the C-C bonds L_1 or L_2 tilted by 30° or 150° from the x axis. The region of the scan line (broken line) is $x_s \geqslant 0$ and $y_s = 3.7c_0$. Each dot is the tip-atom position, the solid circle is a carbon atom, the open circle is a hollow site, and solid lines represent C-C graphite bonds. Spring constants $k_x = k_y = k =$(a) 2.5, (b) 1.5, (c) 1.0, and (d) 0.25 N/m. ''Stick regions'' appear in (c) and (d).

For the case of $k=2.5$ N/m [Fig. 12(a)], the tip-atom distribution deviates only a little from the scan line within the x-y plane toward the hollow site H_1, H_2, and H_3. Therefore the amplitude of the locus of the tip-atom position along the y direction is small. As the cantilever becomes softer ($k=1.5$ N/m [Fig. 12(b)]), the tip-atom position shifts closer to H_1, H_2, and H_3. Therefore the amplitude of the locus of the tip-atom position along the y direction becomes large. This continuous tip-atom motion, which goes beyond the C-C bonds L_1 (L_2) toward H_2 (H_3), produces the zigzag patterns mentioned in Sec. III B 2. For $k=1.0$ N/m [Fig. 12(c)], the gap of the tip-atom distribution appears and the tip atom exists in the regions around H_1, H_2, and H_3. This stick-slip motion of $H_1 \rightarrow H_2 \rightarrow H_3$ produces the zigzag patterns.

However, for the very soft cantilever ($k=0.25$ N/m [Fig. 12(d)]), the tip atom is located very close to the hollow site, and the tip-atom motion $H_1 \rightarrow H_2 \rightarrow H_3$ turns into $H_1 \rightarrow H_3$. In this case, the position where the tip atom sticks just before it slips to H_3 is approximately closer to H_3 than H_2, that is to say, the potential barrier of the C-C bond L_3 becomes lower than that of L_1. In this case the zigzag pattern vanishes.

Thus the variation of the image pattern is explained by the two-dimensional tip-atom behavior.

5. The mechanism of the stick-slip

The mechanism of stick-slip motion in our system is analyzed quantitatively in this section, based on the spatial variation of the total energy V. The concept of this mechanism is based on Tomlinson's picture,[28] and is also similar to that proposed by McClelland[13] or Tomanek, Zhong, and Thomas.[18,19] As an example, the total potential V for $k=0.5$ N/m is calculated as a function of x and z, for each lever basal position x_s, on the broken line of Fig. 3; V can be regarded as $V(x,z;x_s)$ by the symmetry. Figures 13(a)–13(d) represent the case for $x_s=0$ (a), 1.23 (b) ($=c_0/2$), 2.09 (c), and 2.46 Å (d) ($=c_0$). The black circle corresponds to the

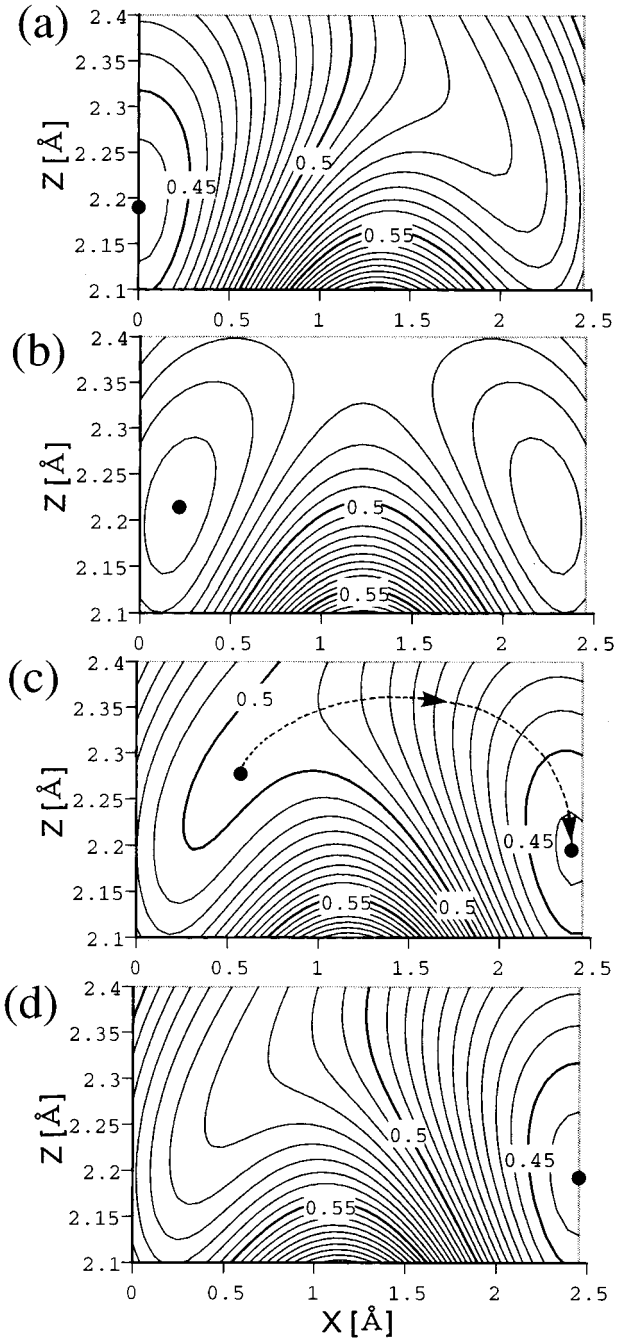

FIG. 13. Two-dimensional adiabatic potential surface $V(x,z;x_s)$ for a contour plot expression. The black circle corresponds to the tip-atom position. x_s is (a) 0, (b) 1.23($=c_0/2$), (c) 2.09, and (d) 2.46($=c_0$) Å.

tip-atom position. First, for $x_s=0$ Å, the tip atom is caught by the minimum of V at the hollow site [Fig. 13(a)]. Then, for $x_s=c_0/2$ Å, V has two minima, which are located symmetrically with respect to $x=c_0/2$ Å [Fig. 13(b)]. The tip atom cannot jump the energy barrier at $x=c_0/2$ Å. Therefore the tip atom is still stuck to the region around the hollow site, and moves only minutely. However, for $x_s=2.09$ Å, the barrier trapping the tip atom disappears and the tip atom moves along the dotted curve toward the deeper minimum [Fig. 13(c)]. This dotted path neglects the variation of the potential surface by the motion of the tip atom. Thus the tip atom slips

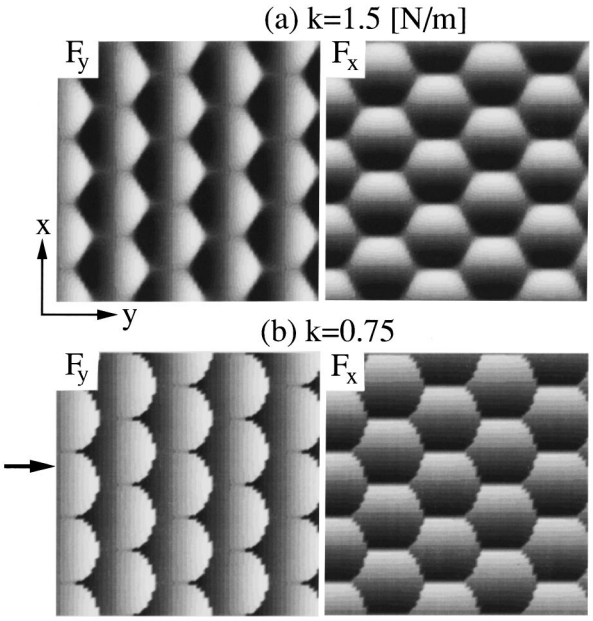

FIG. 14. Lateral force images of F_y and F_x with the tip scanned in the y direction of Fig. 3. Cantilever spring constants $k_y=k_x=k=$(a) 1.5 and (b) 0.75 N/m. The scanning region is 9.9 Å×9.8 Å.

discontinuously between the nearest-neighboring hollow sites towards the scanning direction, and a sudden energy dissipation occurs. This mechanism of energy dissipation is only an assumption we made, mentioned in Sec. II. For $x_s=c_0$ Å, it is clearly shown that the tip atom is caught by the hollow site next to the initial hollow site in the x direction [Fig. 13(d)]. This stick-slip process is repeated with the period of c_0. On the other hand, for the $-x$ scan in Fig. 3, the tip atom takes a similar stick-slip motion symmetrically with respect to $x=c_0/2$ Å. In this case, the position where the atom starts to jump appears at $x_s=0.368$ Å.

C. Scan directional dependence

Lateral force images for other scan directions are calculated, and the dependence of the image by the scan direction is investigated. First, the scan direction is rotated 90° from the one mentioned before: the tip is scanned in the y direction as shown in Fig. 3. Calculated images for $k=1.50$ and 0.75 N/m are shown in Figs. 14(a) and 14(b), respectively. Figure 14(a) is an image of the conservative force, and it is just the same as Fig. 6(b). Please note the direction of the x and y axes. However, the nonconservative force image is clearly different from the corresponding one of before, as exemplified by the difference between Fig. 14(b) and Fig. 6(d).

Then, F_y and F_x in Fig. 15 are the cross sections of Fig. 14(b) over the scan line indicated by the arrow. F_y and F_x mean the lateral force curves of y_s-$F_y(y_s)$ and y_s-$F_x(y_s)$ relations, respectively. The left-hand vertical axis means F_y or F_x, and the right-hand one means the cantilever deflection, $F_y(y_s)/k$ or $F_x(y_s)/k$. F_y exhibits the sawtooth behavior with the periodicity $3b_0/2$, while F_x takes the square-wave behavior, whose rise and fall are synchronized with the sharp slip in the sawtooth behavior of F_y. These behaviors

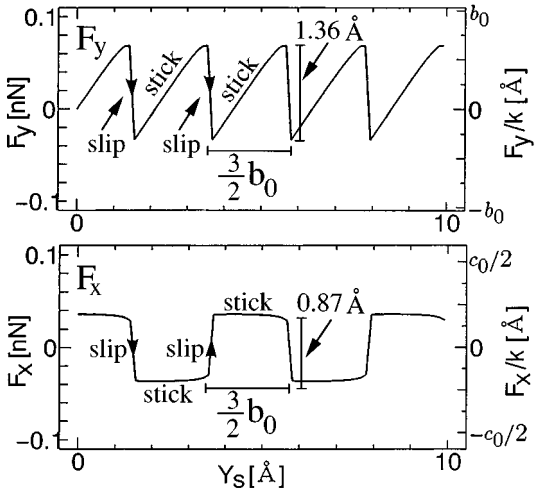

FIG. 15. The cross sections of Fig. 14(b) at the line indicated by the arrow along the y direction. F_y and F_x mean lateral force curves of y_s-$F_y(y_s)$ and y_s-$F_x(y_s)$ relations, respectively. Spring constants $k_x=k_y=k=0.75$ N/m. The left-hand vertical axis means F_y or F_x, and the right-hand one means the cantilever deflection, $F_y(y_s)/k$ or $F_x(y_s)/k$. The tip is scanned in the y direction. c_0 and b_0 are the same as those in Fig. 3. $c_0=2.46$ Å, and $b_0=1.42$ Å.

indicate the two-dimensional zigzag stick-slip of the tip atom between the stick region. Similarly to the case for the x scan in Fig. 6(e), the lateral force image in Fig. 14(b) and the force curve in Fig. 15 agree very well with experimental results by Fujisawa *et al.*[7] [see Fig. 1(a) and Fig. 2(a) in Ref. 7, respectively]. F_x has an image pattern of honeycomb type, and F_y is a wavelike stripe image parallel to the x axis. This agreement is also qualitative, similarly to the case of Fig. 6(e).

Next, the tip atom is scanned in the X direction as shown in Fig. 3. The X axis is obtained by rotating the x axis 15° counterclockwise around the origin (hollow site). The image for $k_X=k_Y=0.75$ N/m is presented in Fig. 16. This nonconservative force image depends remarkably on the scan direction. Thus, it is a general feature that the nonconservative force images significantly vary with the scan direction.

This scan directional dependence together with the anisotropic cantilever was also discussed in relation to the cantilever stiffness by Gyalog *et al.*[20] We will also discuss the influence of the anisotropy of the cantilever in the next section.

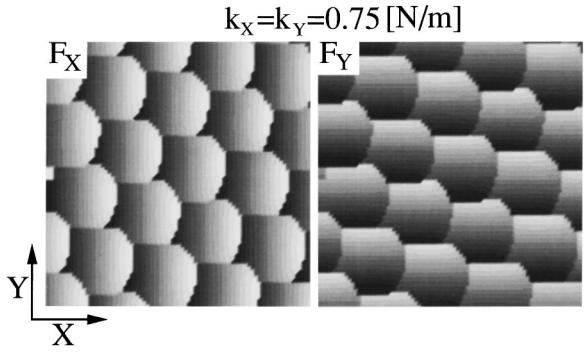

FIG. 16. Lateral force images of F_X and F_Y with the tip scanned in the X direction of Fig. 3. Cantilever spring constants $k_X=k_Y=0.75$ N/m. The scanning region is 10 Å×10 Å.

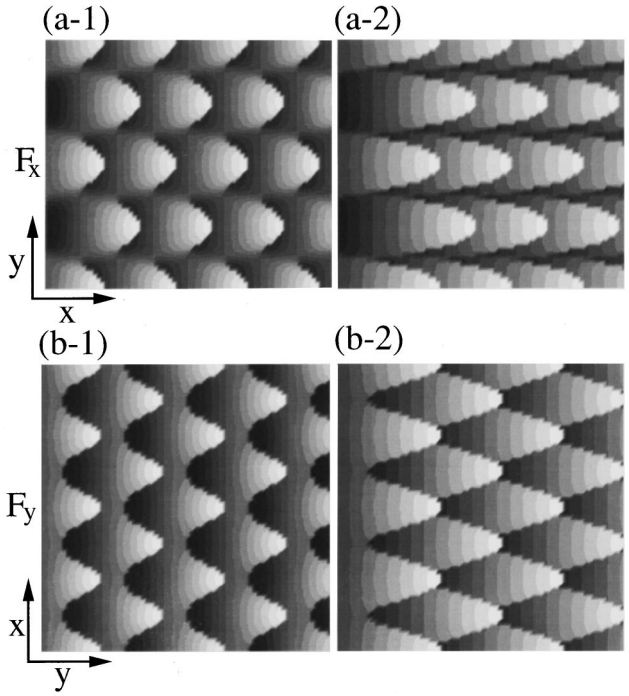

FIG. 17. (a) Lateral force F_x images, with the tip scanned in the x direction of Fig. 3, and (b) F_y images with the y scan. Spring constants (k_x,k_y)=(a-1) (0.50, 5.0), (a-2) (0.25, 2.5), (b-1) (10.0, 0.50), and (b-2) (2.5, 0.25).

D. Anisotropy of the cantilever

The lateral force images are calculated for the case of $k_x \neq k_y$, to see the effect of the anisotropy of the cantilever. First, the tip atom of the cantilever with $k_x < k_y$ is scanned in the x direction of Fig. 3. The images of F_x are presented in Figs. 17(a-1) and 17(a-2). Figure 17(a-1), for $(k_x,k_y)=(0.50, 5.0)$, has a sharper shape in the x direction than the corresponding F_x image in Fig. 6(e) for $(k_x,k_y)=(0.50, 0.50)$. Similarly, Fig. 17(a-2), for $(k_x,k_y)=(0.25, 2.5)$, has a sharper shape in the x direction than the corresponding F_x image in Fig. 6(f), for $(k_x,k_y)=(0.25, 0.25)$. The reason why the sharp image in the x direction appears can be qualitatively explained as follows: Suppose that the lever basal position is scanned in the x direction, on the line that a distance d from the stick region. In this case, the cantilever deflection Δy in the y direction can be approximately regarded as d. Therefore, as d increases for the same x_s, the lateral force $F_y(=k_y d)$ increases rapidly because $k_x < k_y$, and the tip atom can slip more easily in the x direction. Thus the image as shown in Fig. 17(a-1) and 17(a-2) are obtained.

Next, we consider the y scan for the tips with $k_x > k_y$: $(k_x,k_y)=(10.0, 0.50)$ and $(2.5, 0.25)$. The images of F_y are presented in Figs. 17(b-1) and 17(b-2). In these cases, the images sharp in the y direction appear as shown in Fig. 17(b-1) and 17(b-2), by the similar reason mentioned above. In particular, the wavelike pattern of Fig. 17(b-1) is qualitatively in good agreement with that of the experimental image obtained by Ruan and Bhushan[5] [see Fig. 6(a) in Ref. 5]. Thus, by considering the anisotropic cantilever, the direction where the tip atom can easily move appears, and the image becomes sharp toward that direction. Therefore the image by an anisotropic cantilever is considerably different from that by an isotropic one. It can be thought that most of the experimental images might be influenced by an anisotropic spring, which is the sum of the elasticity of the macroscopic cantilever and the microscopic interatomic bonds of the tip.

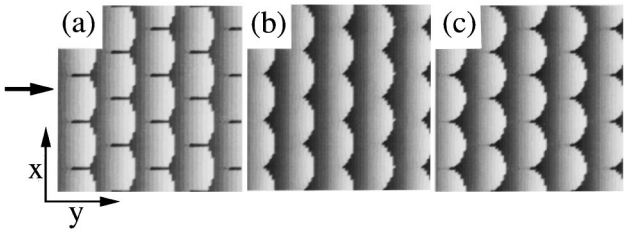

FIG. 18. The comparison of lateral force F_y image for the elastic surface, with those for the rigid surface. The tip is scanned in the y direction on a (a) rigid surface for $k=0.50$ N/m, (b) elastic surface for $k=0.50$ N/m, and (c) rigid surface for $k=0.75$ N/m. The scanning region is 9.9 Å×9.8 Å.

E. Surface deformation

Finally, we allow the graphite surface to deform, using the surface potential V_S, formula (3) in Sec. II. The lateral force images with the y scan are presented as shown in Figs. 18(a)–18(c). Figure 18(b) is an image of an elastic surface for $k_x=k_y=k=0.50$ N/m. Figures 18(a) and 18(c) are images of rigid surfaces for $k=0.50$ and 0.75 N/m, respectively. As seen in these force images, Fig. 18(b) is more similar to Fig. 18(c) than to Fig. 18(a). This feature is quantitatively examined in the cross sections of Figs. 18(a)–18(c) at the line indicated by the thick arrow along the y direction. In Fig. 19, the lateral force curve with $k=0.50$ N/m for an elastic surface takes a behavior similar to that with $k=0.75$ N/m for a rigid surface. Therefore, the surface deformation makes the cantilever effectively stiff. This feature can be explained based on the behavior of the total energy V as follows. The elastic energy of the cantilever V_T does not depend on whether the surface is rigid or elastic. On the other hand, the spatial variations of the tip-surface interaction potential V_{TS} become reduced when the surface deformation is introduced. This is because when the tip atom approaches the potential barrier of V_{TS}, the nearby surface atoms will be relaxed to lower the value of V_{TS}. The degree of the stick-slip is determined by the ratio between the magnitudes of spatial varia-

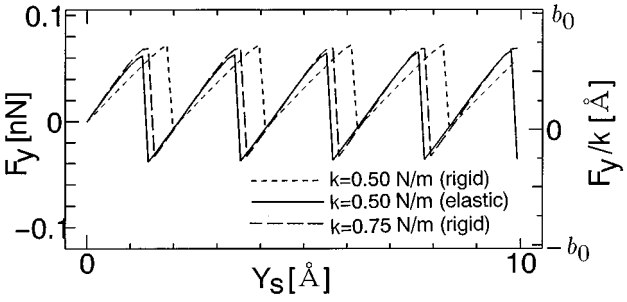

FIG. 19. The cross sections of Fig. 18 at the line indicated by the arrow along the y direction. The dotted, solid, and broken lines correspond to (a) rigid surface for $k=0.50$ N/m, (b) elastic surface for $k=0.50$ N/m, and (c) rigid surface for $k=0.75$ N/m, respectively.

tion of V_T and V_{TS}, as mentioned in Sec. II. Therefore, in this particular case of Fig. 18(b), the ratio V_T/V_{TS} for the elastic surface becomes larger than that for the rigid surface, for the same cantilever or the same V_T. The enhanced ratio can be realized for the stiffer spring for the rigid surface. Thus, it can be said that the effect of elasticity of the surface in the x and y direction is included in the cantilever stiffness k_x and k_y, in the weak loading condition $\langle F_z \rangle \simeq 0.21$ nN of our calculations.

IV. CONCLUSION

In this work, we calculated the lateral force images of the graphite in AFM, and investigated systematically general features of two-dimensional images of atomic-scale frictional force, based on the static calculations. Some of the calculated frictional-force images qualitatively agree well with the observed images. However, the cantilever spring constant k and the load F_z are not reproduced quantitatively. The process in which the weakness of the cantilever spring makes lateral conservative force nonconservative is also clarified from the transition of the lateral force image patterns. On the specific scan line, the critical value of cantilever stiffness k_c is about 1.3 N/m. It is made clear that, for $k < k_c$, the discrete ''stick regions'' appear around the hollow sites. The relation between the image pattern and the arrangement of the graphite atom is discussed. We find that, in the case of the soft cantilever, super structure images appear, and their phase is determined by the initial condition, i.e., the start line of the scan. It is also shown that the scan direction has a significant influence on the nonconservative lateral force image. Further, in the case of the anisotropic cantilever, the direction where the tip atom hardly moves appears, and the image becomes rather different from that for the isotropic lever. Under the comparatively small load F_z, the effect of elasticity of the surface is included in the cantilever stiffness. Therefore surface deformation makes the cantilever effectively stiff.

There are many problems to be solved. First, only the static feature of friction is discussed in this work. However, dynamics of atoms in the cantilever and the surface under the finite temperature $T \neq 0$ K must be included in order to examine the rate of the energy dissipation and its effects on the frictional force. Next, cantilever spring constants k_x and k_y used in our calculation are by two or three orders of magnitude smaller than those in experiments. Two speculations about this problem were presented in Sec. III B 1. One reason is that we use a single-atom tip model. Therefore the tip detects much smaller force than the experimental one, which allows us to use a weak spring. The other reason is that the effective spring constant can become small during the scanning process by the flexing of the tip apex pointed out by Griffith and Grigg.[27] This problem must be considered with the use of more realistic AFM and lateral force models. The scan directional dependence of critical stiffness k_c will give us further understanding of the two-dimensional atomic-scale friction. The difference between the constant-height mode and constant-force mode is also an important issue for a quantitative study. Further, the influences of the multiple-atom tip and flake tip on the atomic-scale friction are very interesting. These problems should be further clarified in our future works.

ACKNOWLEDGMENTS

This work was partially supported by a Grant-in-Aid from the Ministry of Education, Science and Culture of Japan. The numerical calculations were performed by HITAC S-820 and S-3800 at the Computer Center of the University of Tokyo.

[1] G. Binnig, C. F. Quate, and Ch. Gerber, Phys. Rev. Lett. **56**, 930 (1986).
[2] C. M. Mate, G. M. McClelland, R. Erlandsson, and S. Chiang, Phys. Rev. Lett. **59**, 1942 (1987).
[3] H. Heinzelmann, E. Meyer, D. Brodbeck, G. Overney, and H.-J. Güntherodt, Z. Phys. B **88**, 321 (1992).
[4] S. J. O'Shea, M. E. Welland, and T. M. H. Wong, Ultramicroscopy **52**, 55 (1993).
[5] J. Ruan and B. Bhushan, J. Appl. Phys. **76**, 5022 (1994).
[6] J. Ruan and B. Bhushan, J. Appl. Phys. **76**, 8117 (1994).
[7] S. Fujisawa, E. Kishi, Y. Sugawara, and S. Morita, Tribo. Lett. **1**, 121 (1995).
[8] R. Erlandsson, G. Hadziioannou, C. M. Mate, G. M. McClelland, and S. Chiang, J. Chem. Phys. **89**, 5190 (1988).
[9] S. Fujisawa, Y. Sugawara, S. Ito, S. Mishima, T. Okada, and S. Morita, Nanotechnology **4**, 138 (1993).
[10] C. A. J. Putman, M. Igarashi, and R. Kaneko, Appl. Phys. Lett. **66**, 3221 (1995).
[11] S. Fujisawa, E. Kishi, Y. Sugawara, and S. Morita, Phys. Rev. B **51**, 7849 (1995).
[12] J. Kerssemakers and J. Th. M. De Hosson, Appl. Phys. Lett. **67**, 347 (1995).
[13] G. M. McClelland, in *Adhesion and Friction*, edited by M. Grunze and H. J. Kreuzer (Springer-Verlag, Berlin, 1990), pp. 1–16.
[14] U. Landman and W. D. Luedtke, J. Vac. Sci. Technol. B **9**, 414 (1991).
[15] J. A. Harrison, C. T. White, R. J. Colton, and D. W. Brenner, Phys. Rev. B **46**, 9700 (1992).
[16] J. N. Glosli and G. M. McClelland, Phys. Rev. Lett. **70**, 1960 (1993).
[17] W. Zhong and D. Tomanek, Phys. Rev. Lett. **64**, 3054 (1990).
[18] D. Tomanek, W. Zhong, and H. Thomas, Europhys. Lett. **15**, 887 (1991).
[19] D. Tomanek, in *Scanning Tunneling Microscopy III*, edited by R. Wiesendanger and H.-J. Güntherodt (Springer-Verlag, Berlin, 1993), pp. 269–291.
[20] T. Gyalog, M. Bammerlin, R. Luthi, E. Meyer, and H. Thomas, Europhys. Lett. **31**, 269 (1995).
[21] A. Yoshimori and Y. Kitano, J. Phys. Soc. Jpn. **2**, 352 (1956).
[22] S. A. C. Gould, K. Burke, and P. K. Hansma, Phys. Rev. B **40**, 5363 (1989).
[23] N. Sasaki and M. Tsukada, Jpn. J. Appl. Phys. **34**, 3319 (1995).
[24] N. Sasaki and M. Tsukada, Phys. Rev. B **52**, 8471 (1995).

[25] W. H. Press, S. A. Teukolsky, W. T. Vetterling, and B. P. Flannery, *Numerical Recipes: The Art of Scientific Computing*, 2nd ed. (Cambridge University Press, New York, 1992), pp. 413–418.

[26] F. F. Abraham and I. P. Batra, Surf. Sci. **209**, L125 (1989).

[27] J. E. Griffith and D. A. Grigg, J. Appl. Phys. **74**, R83 (1993).

[28] G. A. Tomlinson, Philos. Mag. **7**, 905 (1929).